Editors' Suggestion   Featured in Physics

Tilted Electron Pulses

Dominik Ehberger,[1,2] Andrey Ryabov,[1,2] and Peter Baum[1,2,3,*]

[1]*Ludwig-Maximilians-Universität München, Am Coulombwall 1, 85748 Garching, Germany*
[2]*Max-Planck-Institute of Quantum Optics, Hans-Kopfermann-Str. 1, 85748 Garching, Germany*
[3]*Universität Konstanz, Universitätsstr. 10, 78467 Konstanz, Germany*

We report the all-optical generation and characterization of tilted electron pulses by means of single-cycle terahertz radiation at an electron-transmitting mirror at slanted orientation. Femtosecond electron pulses with a chosen tilt angle are produced at an almost arbitrary target location. The experiments along with theory further reveal that the pulse front tilt in electron optics is directly connected to angular dispersion. Quantum mechanical considerations suggest that this relation is general for particle beams at any degree of coherence. These results indicate that ultrashort electron pulses can be shaped in space and time as versatilely as femtosecond laser pulses, but at 10^5 times finer wavelength and subnanometer imaging resolution.

Ultrashort electron pulses allow the direct visualization of atomic and electronic motion during matter transformations in space and time. For generating the necessary few-femtosecond and attosecond electron pulses, technology is currently progressing from microwave electronics to an all-optical control regime, where the optical cycles of laser-generated radiation are used to steer the electrons in a direct and jitter-free way, obviating the need for active synchronization electronics. So far, ultrashort electron pulses have been accelerated [1], compressed [2,3], energy-modulated [4], and streaked [2,5] by all-optical approaches, but many applications require more complex phase-space correlations involving multiple dimensions.

Here, we report a multidimensional, dynamical control of electron pulses by all-optical means, exemplified by the generation and characterization of tilted electron pulses. Such pulses, propagating non-normally to their pulse front, promise to improve free-electron laser performance [6] and enable pump-probe experiments in which optical cycles are used for sample excitation [7,8].

Our concept [Fig. 1(a)] is based on the controlled phase-space modulation of a beam of electrons (blue) by the cycles of electromagnetic radiation (red). The interaction is mediated by an ultrathin metal mirror (dark gray) in an off-angle geometry. Electrons can pass through, but radiation is reflected. The electrons therefore obtain a net momentum change from the optical cycles due to their passage through the mirror material within subcycle time [9]. For generating tilted electron pulses with multidimensional correlations in space and time, we place the mirror in such a way in the optical beam that different lateral slices of the electron beam are accelerated or decelerated with a constant gradient across the beam. Simultaneously, we ensure that the entire beam is uniformly compressed in time [2].

Therefore, we expect ultrashort and tilted pulses on a target after free-space propagation.

In order to find the appropriate geometry, we treat the electron beam classically and assume a point charge e of initial velocity $v_e = \beta c$ along the z axis (initial momentum p_z and $p_y = 0$) that is passing through a perfect mirror ($y = z = 0$) irradiated with a p-polarized plane wave (angular frequency ω, peak field strength E_0 at $y = z = t = 0$) as an approximation for the fields in the waist of a Gaussian beam (full width at half maximum w_0, Rayleigh length z_R; $z_R \gg w_0$). The mirror reflection causes a moving interference pattern with magnetic and electric contributions. An analytic derivation (see Supplemental Material [12]) provides the transverse and longitudinal momentum transfer components Δp_y and Δp_z after the interaction

$$\Delta p_{y,z}(t) = eE_0 A_{y,z}(\theta_e, \theta_{\text{THz}}, \beta) \frac{\sin(\omega t)}{\omega}. \quad (1)$$

Here, t is the arrival time of the electron at the mirror. The amplitude of this sinusoidal momentum modulation depends on the angles θ_e and θ_{THz} [see Fig. 1(b)] via the geometry factors

$$A_y = \pm \left(\frac{\cos(\theta_e + \theta_{\text{THz}}) + \beta}{1 + \beta \cos(\theta_e + \theta_{\text{THz}})} - \frac{\cos(\theta_e - \theta_{\text{THz}}) - \beta}{1 - \beta \cos(\theta_e - \theta_{\text{THz}})} \right), \quad (2)$$

$$A_z = \pm \left(\frac{\sin(\theta_e - \theta_{\text{THz}})}{1 - \beta \cos(\theta_e - \theta_{\text{THz}})} - \frac{\sin(\theta_e + \theta_{\text{THz}})}{1 + \beta \cos(\theta_e + \theta_{\text{THz}})} \right), \quad (3)$$

where the positive (negative) sign is for the same (opposite) incidence of the electrons and the plane wave with respect
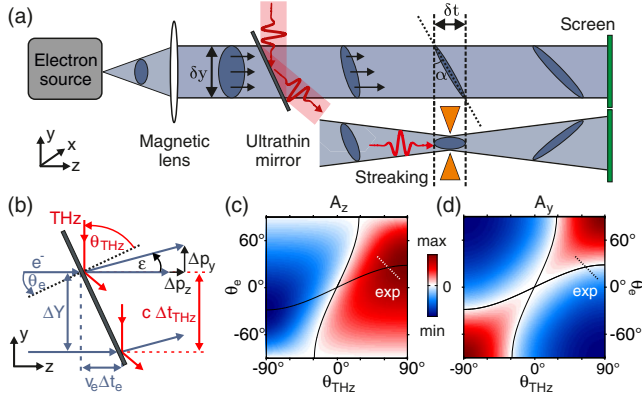
FIG. 1. All-optical generation of tilted electron pulses. (a) Concept and experiment. Electron pulses (blue) pass through a mirror (dark gray) that is irradiated by single-cycle terahertz radiation (red). A traveling interference pattern along the mirror surface converts the electrons into compressed and tilted pulses. (Lower) If the electron beam is focused with the magnetic lens, the tilt angle increases with decreasing beam size, with the opposite sign after its waist. A terahertz-driven resonator (orange) and a phosphor screen (green) provide the necessary metrology to reveal this tilting dynamics by experiment. (b) Definition of angles for the analytical derivations. (c) Amplitude of the longitudinal momentum change as a function of the geometry. (d) Amplitude of the transverse momentum change. (Dotted lines) Angle combinations applied in the experiments; (solid lines) zero-deflection conditions.

to the mirror. The momentum gain is assumed to be small compared to the initial momentum ($\Delta p_{y,z} \ll p_z$) and ponderomotive effects are neglected. Under these assumptions, Eqs. (1)–(3) hold for relativistic particles, too.

We find that acceleration and deflection are in phase with each other, regardless of the angles. Furthermore, both momentum changes are phase shifted by $\pi/2$ with respect to the incident electromagnetic wave. Therefore, cosinelike optical pulses (carrier-envelope phase of zero) lead to sinelike electron momentum modulation (carrier-envelope phase of $\pi/2$) and vice versa. Terahertz pulses from optical rectification typically have a carrier-envelope phase of zero in a focus [10,11] and therefore provide a sinusoidal momentum modulation. This time dependency of Δp_z causes pulse compression by deceleration of the incoming pulse's earlier parts and acceleration of the later parts. Thus, only half an optical cycle is responsible for compression, and in case of pulses, the relevant part of the momentum kick can be approximated by a modulation with a single frequency ω (see Supplemental Material [12]). If an incoming electron pulse is shorter than the optical half-cycle, we obtain isolated electron pulses [2], otherwise pulse trains [5,13,14]. The minimum pulse duration is achieved at the temporal focus $f_{\text{temp}} = (\beta^2 \gamma^3 / A_z E_0)(m_e c^2 / e)$ (see Supplemental Material [12]); m_e is the electron mass and γ is the Lorentz factor. Analogously, there is a time-dependent sideways deflection

via $\Delta p_y \propto A_y$, which allows us to realize a cathode ray oscilloscope at optical frequencies [2,5].

The geometry factors A_z and A_y are plotted in Figs. 1(c) and 1(d) for electrons with a kinetic energy of 70 keV. We find that there are certain combinations of angles for which $\Delta p_y = 0$, that is, no net deflection after interaction. This effect is due to cancellation of electric and magnetic contributions and occurs for $\sin \theta_{\text{THz}} = \beta \sin \theta_e$ and $\sin \theta_{\text{THz}} = \beta^{-1} \sin \theta_e$ [Figs. 1(c) and 1(d), solid lines]. For most other angular configurations, we find that deflection and acceleration occur simultaneously, providing opportunity for multidimensional control. The dotted lines mark a convenient region for pulse front tilting experiments, because the deflection is weak there and the compression strength is roughly constant when varying the slant angle of the mirror. The position of the temporal focus is therefore approximately independent of angular adjustments.

For electron beams with a finite diameter, certain angular configurations provide velocity matching [9], that is, all electrons have the same relative delay to the optical cycles regardless of their position within the beam [Fig. 1(b)]. Velocity matching is achieved if

$$\frac{c}{\sin \theta_{\text{THz}}} = \frac{v_e}{\sin \theta_e}, \tag{4}$$

that is, if the superluminal phase velocity of the optical interference pattern along the mirror surface equals the surface velocity of the electron pulse's point of incidence. In order to generate tilted electron pulses, we rotate the mirror away from this velocity-matching condition. This simple adjustment produces a lateral timing mismatch $\Delta T = \Delta t_{\text{THz}} - \Delta t_e$ between the optical cycles and electrons of different beam positions ΔY [Fig. 1(b)]. Considering the geometry depicted in Fig. 1(b), we obtain

$$\frac{\Delta T}{\Delta Y} = \frac{\sin \theta_{\text{THz}}/c - \sin \theta_e / v_e}{\cos \theta_e}. \tag{5}$$

If the position-dependent delay is smaller than a half-period of the optical radiation, the momentum modulation is nearly linear in space and time. Therefore, incoming electron pulses obtain a position-dependent overall acceleration or deceleration in addition to the time-dependent longitudinal momentum modulation that causes compression. Consequently, there is a constant velocity-gain gradient along the transverse beam profile [Fig. 1(a)] and different slices of the beam profile arrive earlier or later at the target, that is, as tilted pulses. The lateral arrival time difference of $\delta t/\delta y$ results in a tilt angle $\alpha = \tan^{-1}(v_e \delta t/\delta y)$ for a collimated beam [Fig. 1(a)]. At the temporal focus, we find $\delta t/\delta y = \Delta T/\Delta Y$ (see Supplemental Material [12]) and thus

$$\tan \alpha = v_e \frac{\Delta T}{\Delta Y}. \qquad (6)$$

We see that the tilt angle in the temporal focus is solely determined by the combined sweeping dynamics of the electrons and the terahertz cycles across the mirror and is not dependent on the applied optical field strength or its wavelength. According to Eq. (6), compressed electron pulses can be produced at almost arbitrary tilt angle α and position f_{temp}, simply by rotating the mirror for the tilt and adjusting the optical field strength for the temporal focus position.

In the experiment, we use single-cycle terahertz pulses (central frequency 0.3 THz [10]) as control fields. The mirror element is a 10-nm Al layer on a 10-nm SiN membrane (size 1.5×1.5 mm^2) with a reflectivity of >90% [15]. The transmission of our 70-keV electron pulses [16] is $\sim 70\%$. Space charge effects are avoided by using <5 electrons per pulse [17] at a repetition rate of 50 kHz. We let the terahertz beam cross the electron beam approximately at 90° [see Fig. 1(a)]. Finite transverse beam size effects of the electromagnetic wave can be neglected, because the electron beam diameter (<1 mm) is much smaller than w_0 (~ 3 mm) or z_R (~ 2 cm) of the terahertz pulses. The incident peak electric field strength is $\sim 2 \times 10^5$ V/m, which produces a temporal focus at $f_{temp} \approx$ 0.5 m and compresses the electron pulses from 1 ps to ~ 100 fs. For pulse tilt characterization, we use a magnetic solenoid lens that creates an intermediate waist [Fig. 1(a), lower panel] and therefore a shadow image of the mirror on the screen (green). The half-angle divergence of the electron beam at the mirror is ~ 1 mrad. A butterfly shaped metal resonator (orange) is placed at the waist position, which coincides with the temporal focus. It is illuminated with a second terahertz pulse [11] at $\sim 9 \times 10^5$ V/m peak field strength and serves as a streaking element, that is, it deflects the electrons along the x axis [out of the plane in Fig. 1(a)] as a function of arrival time [2]. This streaking metrology in combination with the shadow imaging allows us to determine the arrival time differences δt between different parts of the beam profile along y, in order to measure the pulse front tilt of a collimated beam [Fig. 1(a), upper panel].

Figure 2(a) shows raw screen images (each at a zero crossing of the streaking field) for different slant angles of the mirror. The apparent shear in the data directly demonstrates the predicted arrival time differences between electrons originating from different points of the foil (dashed lines) and thus shows that tilted electron pulses are produced.

A quantitative analysis is obtained by recording a series of screen images while scanning the streaking delay (for details see Supplemental Material [12]). This metrology reveals a time-dependent streaking trace for each position y in the electron beam [Fig. 2(b)]. We see that each slice of the beam deflects with a sinusoidal dependency in
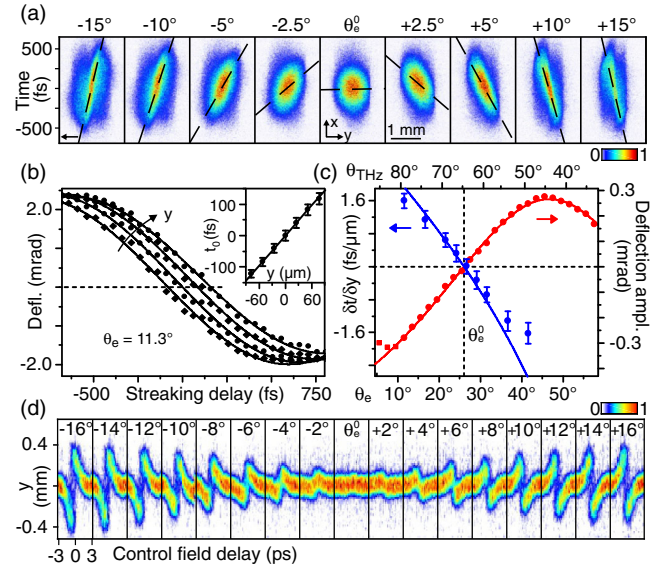

FIG. 2. Experimental results on tilted electron pulses. (a) Screen images for different mirror slant angles at the zero crossing of the streaking field. Scale bar, 1 mm. The pulse front tilt is evident from the measured lateral arrival time differences (dashed line, time axis). (b) Streaking traces (dots and diamonds) for different y positions within the beam profile and sinusoidal fitting curves (solid). (Inset) Time zero of the streaking traces. (c) Measured arrival time difference (blue dots) and deflection amplitude (red dots). Red line, fit by Eq. (2); squares are excluded. Blue line, prediction by Eq. (5). Error bars indicate one standard deviation. (d) Time-dependent deflection measurements (deflectograms) for different mirror slant angles.

time, following the half-cycle of the terahertz streaking field with a position-dependent delay (see inset). The slope of this measured delay is $\delta t / \delta y$ for the chosen mirror angle ($\theta_e = 11.3°$ in the figure). Repetition of this procedure for all angles provides the blue dots in Fig. 2(c), showing the measured lateral arrival time differences $\delta t / \delta y$ as a function of θ_e and θ_{THz}.

In a second, independent experiment, we determine the relative strength of the transverse momentum kick Δp_y as a function of the mirror angle. To this end, the streaking element is removed and beam position changes are recorded as a function of the terahertz delay at the mirror. An aperture close to the foil (diameter 50 μm) decreases the beam diameter and a peak field strength of $\sim 4 \times 10^5$ V/m further enhances the resolution. Figure 2(d) shows a subset of the measured deflectograms [2] as a function of the mirror angle. The observed time-dependent deflections are proportional to $\Delta p_y(t)$. We see that all traces are single cycle and sinelike, as expected from our cosinelike terahertz pulses [10] via the considerations above. The peak-to-peak amplitude is proportional to the geometry factor A_y for sideways momentum transfer and shows a strong dependency on the mirror slant angle [red dots in Fig. 2(c)].
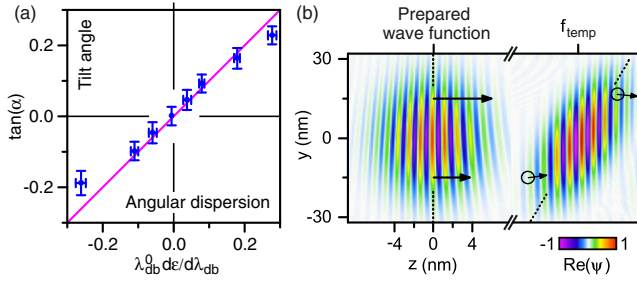
FIG. 3. Pulse front tilt vs angular dispersion for electrons, and quantum simulations. (a) Measured angular dispersion in electron pulses as a function of tilt angle (blue) in comparison to this Letter's conjecture [Eq. (7), magenta]. Error bars indicate one standard deviation and are omitted when smaller than a data point. Unequal scanning ranges of the raw data [Fig. 2(c)] are accounted for by linear interpolation. (b) Quantum simulation of an electron wave packet $\psi(z, y, t)$ with initial position-momentum correlation (left) propagated to the temporal focus f_{temp} (right). We assume a coherence time of 8 fs, a beam waist of 20 nm, and a linear transverse change of forward momentum, as from the experiment (black arrows). The electron energy is 1 eV in order to make the de Broglie wavelength visible in the results. The phase fronts remain approximately perpendicular to the propagation direction, but the envelope becomes tilted. Angular dispersion is indicated by the black circles and constant throughout the simulation.

A least-squares fit to the data with Eq. (2) reveals the precise angle $\Delta\theta = \theta_{THz} + \theta_e$ between the electrons and the terahertz beam in the experiment, as well as a proportionality constant C that includes the screen distance and electric peak field strength. We obtain $\Delta\theta = (93.4 \pm 0.8)°$. The result is plotted as a red solid line in Fig. 2(c), which compares very well to the measured data and confirms the validity of the analytical expressions for sideways deflection [Eqs. (1) and (2)]. Using $\Delta\theta$, we compare the measured tilt parameters $\delta t / \delta y$ (blue dots) to $\Delta T / \Delta Y$ via Eq. (5) (blue solid line). We observe a good agreement; deviations at larger angles are attributed to residual shifts of the temporal focus by nonconstant $\Delta p_z(\theta_e, \theta_{THz})$, which is neglected here [see Fig. 1(c), dotted line]. The agreement of the measured tilt data to the theory shows that tilted electron pulses are generated as predicted by Eq. (6).

The two separate experiments on tilt and deflection [blue and red data in Fig. 2(c), respectively] reveal a nontrivial coincidence between the velocity-matching condition and absent deflection. Both data traces cross zero at the same angle θ_e^0, which happens to be the velocity-matching angle according to Eq. (4). It follows that planar elements, if oriented according to Eq. (4), allow compressing electron pulses of arbitrarily large beam diameter by means of all-optical control without any unwanted time-dependent deflections.

Furthermore, we see from Fig. 2(c) that the measured pulse front tilt appears to be linked to the measured

deflection strength: larger tilt angles imply stronger sideways effects. In optics, there is a direct relationship between pulse front tilt and angular dispersion via $\tan\alpha = \bar{\lambda} d\epsilon/d\lambda$ [18], where α is the pulse front tilt, $\bar{\lambda}$ is the spectral mean, and $d\epsilon/d\lambda$ is the angular dispersion (change of deflection angle ϵ per wavelength λ). Our two experiments reveal a similar relation for electrons. We define the angular electron dispersion analogously to the optical case as $d\epsilon/d\lambda_{db}$, where ϵ is the electron deflection angle [Fig. 1(b)] and $\lambda_{db} \approx h/p_z$ is the electron de Broglie wavelength. In order to evaluate $d\epsilon/d\lambda_{db}$ from the data, we assume $p_y \ll p_z$ (paraxial approximation) and constant angular dispersion. Differentiating $\epsilon = p_y/p_z$ and λ_{db} yields $d\epsilon = (1/p_z)[dp_y - (p_y/p_z)dp_z]$, $d\lambda_{db} = -(\lambda_{db}/p_z)dp_z$, and $d\epsilon/d\lambda_{db} = -(1/\lambda_{db})[(dp_y/dp_z) - (p_y/p_z)]$. For $\lambda_{db} = \lambda_{db}^0$, where λ_{db}^0 is the initial de Broglie wavelength of the not-deflected electron ($\epsilon = 0$), we obtain $-\lambda_{db}^0(d\epsilon/d\lambda_{db}) = \Delta p_y/\Delta p_z = [A_y(\theta_e, \theta_{THz})/A_z(\theta_e, \theta_{THz})]$, A_y is obtained from the measured deflection amplitude [red dots in Fig. 2(c)], and A_z is calculated via Eq. (3) by using $\Delta\theta$ and C from the calibration of the setup.

The result of this conversion is reported in Fig. 3(a), where we plot $\lambda_{db}^0(d\epsilon/d\lambda_{db})$ (evaluated angular dispersion) against $\tan\alpha$ (measured tilt strength). We see that all data points are close to a straight line with a slope of unity (magenta). This experimental finding motivates the conjecture

$$\tan\alpha = \lambda_{db}^0 \frac{d\epsilon}{d\lambda_{db}} \qquad (7)$$

for electron pulses in a temporal focus, where all energy components overlap in space and time. Equation (7) is the matter wave analog to its optical counterpart [18].

In contrast to laser pulses, our electron pulses in the experiment have a 10^5 times shorter wavelength, a rest mass, and sublight speed. The beam is also rather incoherent and the electrons behave almost like point particles due to their low degree of coherence of $\sim 10^{-4}$ in space and $\sim 10^{-2}$ in time [17]. Furthermore, our way of generating tilted electron pulses is different from the optical approach, namely, by applying a position-dependent acceleration or deceleration instead of using a passive dispersive element like a prism or a grating. The fact that there is nevertheless an apparent connection between tilt and dispersion in the experiment [see Fig. 3(a)] suggests that Eq. (7) might be general for any type of matter wave at arbitrary degree of coherence.

A simulation of a fully coherent electron wave packet with a transverse momentum modulation is depicted in Fig. 3(b), motivated by recent experimental advances in laser-triggered high-coherence electron sources [19]. We assume an initial electron wave function $\psi(y, z) = \exp[-z^2/(2z_0^2) - y^2/(2y_0^2) + i(k_0 + c_y y)z + ic_z z^2]$, where
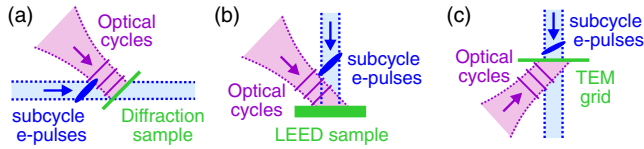
FIG. 4. Potential applications of tilted electron pulses. (a) Subcycle/attosecond electron diffraction [5]. A crystalline sample (green) is oriented along a zone axis for generating multiple Bragg spots. The laser phase front (violet) has a polarization along the crystal surface. Tilted electron pulses (blue) propagate with sublight speed, but probe the sample in synchrony with the field cycles. (b) Subcycle low-energy electron diffraction (LEED). Laser cycles (violet) illuminate a sample material (green) at an angle due to practical space restrictions [26]. Tilted electron pulses (blue) can probe every part of the surface with the same delay with respect to the field cycles. (c) Subcycle electron microscopy. A transmission electron microscopy grid (TEM grid) can usually not be tilted a lot with respect to the twin lens in a high-resolution microscope. Nevertheless, a combination of tilted electron pulses (blue) and diagonal laser incidence (violet) can provide a uniform subcycle-level delay over the entire illuminated TEM grid area.

z_0 is the pulse length, y_0 is the wave packet width, k_0 is the mean wave vector, c_z is the chirp coefficient, and c_y is a y-dependent longitudinal momentum change. Free-space propagation in a nonrelativistic approximation is calculated via Fourier transformation, multiplication with the propagator $\exp[i\hbar k^2 t/(2m_e)]$, and backtransformation; t is the propagation time and k is the electron wave vector. We see [Fig. 3(b)] that the phase fronts are angled to the pulse shape, and different wavelengths travel at different angles (black circles). These simulations support Eq. (7) for the case of fully coherent electron wave packets.

In conclusion, our results show that tilted and compressed electron pulses can efficiently be generated by all-optical means and simple interaction elements. Tilted electron pulses allow for ultrafast pump-probe diffraction and microscopy in which the optical cycles are used for sample excitation or control (see Fig. 4). In experiments where the electron pulses are longer than an optical period [4,5,13,14], the energy sidebands [4,9] will be coupled to the deflection angles [2,5], potentially enabling novel imaging concepts in electron microscopy [4,20]. Tailored optical control fields or more complex interaction elements [21] provide opportunity for complex phase-space manipulations to create exotic beams and pulse shapes at target. We predict that the controlled generation of such electron pulses will enable a wide range of future applications in probing and controlling materials, possibly along with electron vortices and Airy or Bessel beams [22–25].

*peter.baum@uni-konstanz.de

[1] E. A. Nanni, W. R. Huang, K.-H. Hong, K. Ravi, A. Fallahi, G. Moriena, R. J. D. Miller, and F. X. Kaertner, Terahertz-driven linear electron acceleration, Nat. Commun. **6**, 8486 (2015).

[2] C. Kealhofer, W. Schneider, D. Ehberger, A. Ryabov, F. Krausz, and P. Baum, All-optical control and metrology of electron pulses, Science **352**, 429 (2016).

[3] E. Curry, S. Fabbri, J. Maxson, P. Musumeci, and A. Gover, Meter-Scale Terahertz-Driven Acceleration of a Relativistic Beam, Phys. Rev. Lett. **120**, 094801 (2018).

[4] B. Barwick, D. J. Flannigan, and A. H. Zewail, Photon-induced near-field electron microscopy, Nature (London) **462**, 902 (2009).

[5] Y. Morimoto and P. Baum, Diffraction and microscopy with attosecond electron pulse trains, Nat. Phys. **14**, 252 (2018).

[6] E. Prat, F. Lohl, and S. Reiche, Efficient generation of short and high-power x-ray free-electron-laser pulses based on superradiance with a transversely tilted beam, Phys. Rev. ST Accel. Beams **18**, 100701 (2015).

[7] H. C. Shao and A. F. Starace, Detecting Electron Motion in Atoms and Molecules, Phys. Rev. Lett. **105**, 263201 (2010).

[8] V. S. Yakovlev, M. I. Stockman, F. Krausz, and P. Baum, Atomic-scale diffractive imaging of sub-cycle electron dynamics in condensed matter, Sci. Rep. **5**, 14581 (2015).

[9] F. O. Kirchner, A. Gliserin, F. Krausz, and P. Baum, Laser streaking of free electrons at 25 keV, Nat. Photonics **8**, 52 (2014).

[10] M. V. Tsarev, D. Ehberger, and P. Baum, High-average-power, intense THz pulses from a LiNbO3 slab with silicon output coupler, Appl. Phys. B **122**, 30 (2016).

[11] W. Schneider, A. Ryabov, Cs. Lombosi, T. Metzger, Zs. Major, J. A. Fulop, and P. Baum, 800-fs, 330-uJ pulses from a 100-W regenerative Yb:YAG thin-disk amplifier at 300 kHz and THz generation in LiNbO3, Opt. Lett. **39**, 6604 (2014).

[12] See Supplemental Material at http://link.aps.org/supplemental/10.1103/PhysRevLett.121.094801 for analytic derivations and details on data analysis.

[13] K. E. Priebe, C. Rathje, S. V. Yalunin, T. Hohage, A. Feist, S. Schäfer, and C. Ropers, Attosecond electron pulse trains and quantum state reconstruction in ultrafast transmission electron microscopy, Nat. Photonics **11**, 793 (2017).

[14] M. Kozák, N. Schönenberger, and P. Hommelhoff, Ponderomotive Generation and Detection of Attosecond Free-Electron Pulse Trains, Phys. Rev. Lett. **120**, 103203 (2018).

[15] N. Laman and D. Grischkowsky, Terahertz conductivity of thin metal films, Appl. Phys. Lett. **93**, 051105 (2008).

[16] L. Kasmi, D. Kreier, M. Bradler, E. Riedle, and P. Baum, Femtosecond single-electron pulses generated by two-photon photoemission close to the work function, New J. Phys. **17**, 033008 (2015).

[17] P. Baum, On the physics of ultrashort single-electron pulses for time-resolved microscopy and diffraction, Chem. Phys. **423**, 55 (2013).

[18] J. Hebling, Derivation of the pulse front tilt caused by angular dispersion, Opt. Quantum Electron. **28**, 1759 (1996).

[19] D. Ehberger, J. Hammer, M. Eisele, M. Krüger, J. Noe, A. Högele, and P. Hommelhoff, Highly Coherent Electron Beam from a Laser-Triggered Tungsten Needle Tip, Phys. Rev. Lett. **114,** 227601 (2015).

[20] A. Ryabov and P. Baum, Electron microscopy of electromagnetic waveforms, Science **353,** 374 (2016).

[21] D. Zhang, A. Fallahi, M. Hemmer, X. Wu, M. Fakhari, Y. Hua, H. Cankaya, A.-L. Calendron, L. E. Zapata, N. H. Matlis, and F. X. Kärtner, Segmented terahertz electron accelerator and manipulator (STEAM), Nat. Photonics **12,** 336 (2018).

[22] J. Verbeeck, H. Tian, and P. Schattschneider, Production and application of electron vortex beams, Nature (London) **467,** 301 (2010).

[23] N. Voloch-Bloch, Y. Lereah, Y. Lilach, A. Gover, and A. Arie, Generation of electron airy beams, Nature (London) **494,** 331 (2013).

[24] V. Grillo, E. Karimi, G. C. Gazzadi, S. Frabboni, M. R. Dennis, and R. W. Boyd, Generation of Nondiffracting Electron Bessel Beams, Phys. Rev. X **4,** 011013 (2014).

[25] C. L. Zheng, T. C. Petersen, H. Kirmse, W. Neumann, M. J. Morgan, and J. Etheridge, Axicon Lens for Electrons using a Magnetic Vortex: The Efficient Generation of a Bessel Beam, Phys. Rev. Lett. **119,** 174801 (2017).

[26] M. Gulde, S. Schweda, G. Storeck, M. Maiti, H. K. Yu, A. M. Wodtke, S. Schäfer, and C. Ropers, Ultrafast low-energy electron diffraction in transmission resolves polymer/ graphene superstructure dynamics, Science **345,** 200 (2014).